Biochemical and Biophysical Research Communications 450 (2014) 991–997

Contents lists available at ScienceDirect

Biochemical and Biophysical Research Communications

journal homepage: www.elsevier.com/locate/ybbrc

Electron microscopy and *in vitro* deneddylation reveal similar architectures and biochemistry of isolated human and Flag-mouse COP9 signalosome complexes

Beate Rockel [a], Tilo Schmaler [b], Xiaohua Huang [b], Wolfgang Dubiel [b,*]

[a] Department of Molecular Structural Biology, Max-Planck-Institute of Biochemistry, Am Klopferspitz 18, 82152 Martinsried, Germany
[b] Division of Molecular Biology, Department of General, Visceral, Vascular and Thoracic Surgery, Charité – Universitätsmedizin Berlin, Charitéplatz 1, 10117 Berlin, Germany

ARTICLE INFO

Article history:
Received 3 June 2014
Available online 25 June 2014

Keywords:
COP9 signalosome
Lid
Deneddylation
Cryo-electron microscopy
3D-reconstruction
Single-particle analysis

ABSTRACT

The COP9 signalosome (CSN) is a regulator of the ubiquitin (Ub) proteasome system (UPS). In the UPS, proteins are Ub-labeled for degradation by Ub ligases conferring substrate specificity. The CSN controls a large family of Ub ligases called cullin-RING ligases (CRLs), which ubiquitinate cell cycle regulators, transcription factors and DNA damage response proteins. The CSN possesses structural similarities with the 26S proteasome Lid complex and the translation initiation complex 3 (eIF3) indicating similar ancestry and function. Initial structures were obtained 14 years ago by 2D electron microscopy (EM). Recently, first 3D molecular models of the CSN were created on the basis of negative-stain EM and single-particle analysis, mostly with recombinant complexes.

Here, we compare deneddylating activity and structural features of CSN complexes purified in an elaborate procedure from human erythrocytes and efficiently pulled down from mouse Flag-CSN2 B8 fibroblasts. In an *in vitro* deneddylation assay both the human and the mouse CSN complexes deneddylated Nedd8-Cul1 with comparable rates. 3D structural models of the erythrocyte CSN as well as of the mouse Flag-CSN were generated by negative stain EM and by cryo-EM. Both complexes show a central U-shaped segment from which several arms emanate. This structure, called the horseshoe, is formed by the PCI domain subunits. CSN5 and CSN6 point away from the horseshoe. Compared to 3D models of negatively stained CSN complexes, densities assigned to CSN2 and CSN4 are better defined in the cryo-map. Because biochemical and structural results obtained with CSN complexes isolated from human erythrocytes and purified by Flag-CSN pulldown from mouse B8 fibroblasts are very similar, Flag-CSN pulldowns are a proper alternative to CSN preparation from erythrocytes.

1. Introduction

The CSN forms supercomplexes with CRLs and inhibits their ubiquitinating activity by deneddylation [1]. CSN-mediated deneddylation protects CRL components from autoubiquitination and is necessary for their remodeling [2]. This allows adaptation of the UPS to changed substrate specificity requirements.

Initial structural analysis of the CSN complex was published in 2000, where the purified complex from human erythrocytes was investigated using negative-stain EM [3]. In these studies, images of the CSN and the 26S proteasome Lid complex revealed similar architectures. In addition, there is significant structural similarity with the translation initiation complex 3 (eIF3) [4]. In mammalian cells, the three complexes (CSN, Lid and eIF3 also summarized as ZOMES) are composed of six (Proteasome, COP9 signalosome, Initiation factor eIF3) PCI-domain and two (MOV34, Pad1 N-terminal) MPN-domain subunits. Additional progress in the field was recently obtained by EM and single particle analysis, which generated a 3D molecular model for the CSN [5,6]. CSN subunits locations were predicted on the basis of comparison with homologs in the Lid defined by recent EM studies [7,8]. In this model, PCI domains form a horseshoe-shaped complex, from which the extended N-terminal domains radiate. The four largest PCI-subunits (CSN1, CSN2, CSN3, and CSN4) seem to dock into the central region of the arc, which is capped at each end by the shorter PCI-subunits CSN7 and CSN8. The MPN-subunits CSN5 and CSN6 are predicted to generate a protrusion on the side opposite the PCI subunits [6]. Interestingly, this arrangement is reminiscent of the horseshoe-like structure described for the PCI domains of 26S proteasome Lid complex [7].

* Corresponding author. Fax: +49 30 450522928.
E-mail address: Wolfgang.dubiel@charite.de (W. Dubiel).

http://dx.doi.org/10.1016/j.bbrc.2014.06.093
0006-291X/

The JAMM/MPN+ domain protein CSN5 is responsible for the CSN-mediated deneddylation [9]. Free CSN5 is inactive and needs structural rearrangements in the CSN holo-complex for activation [10], analogous to the catalytic subunit of the proteasomal Lid, Rpn11 [11,12]. Kinetic studies [13] revealed that the CSN is an efficient enzyme using neddylated Cul1 as substrate with a k_{cat} of approximately 1 s^{-1} [13].

In recent years, negative-stain models of the CSN were obtained with recombinantly expressed CSN complexes [5,6]. Here we present structural data of native CSN isolated from human erythrocytes confirming former models. Moreover, to switch from the time-consuming (2–3 weeks) procedure of CSN preparation from human erythrocytes to the more efficient (2–3 days) protocol of Flag-CSN pulldown, we characterized CSN complexes obtained from Flag-CSN2 mouse B8 fibroblasts [14]. Obtained results reveal similar architecture and deneddylation activity of CSN complexes isolated from human red blood cells and pulled down from mouse B8 fibroblast.

2. Materials and methods

2.1. Biochemical analyzes

The CSN was isolated from human erythrocytes according to a published protocol [15]. Flag pulldowns were described before [16]. Flag-CSN complexes pulled down from mouse B8 cells stably expressing Flag-CSN2 were eluted from Flag beads (Sigma) and concentrated by Ultracel-30k (Millipore) 10 times. The CSN concentrate was loaded on a density glycerol gradient and centrifuged for 4 h at 60.000 RPM using a TLA 100.3 (Beckman) [17]. CSN-containing fraction (approximately 17–18% glycerol) was used for further analysis. Den1 was subcloned in pGEX4T3 (Amersham) and pQE (Invitrogen) vectors. GST- and His-Den1 were purified under non denaturing conditions. Nedd8-GFP fusion plasmid was kindly provided by Michael Glickman. Purification of Nedd8-GFP was carried out under denaturing conditions according manufacture specifications. Deneddylation of Nedd8-GFP was performed for 30 min at 37 °C in buffer containing 30 mM Tris, 10 mM KCl, 5 mM DTT (pH 7.8). The Cul1 plasmid was obtained from Zeng and Schulman and purified according to a published protocol [18]. *In vitro* neddylation of the construct consisting of Cul1 associated to Rbx1 was performed as described [19]. Residual unconjugated Nedd8 was removed by an additional GST-purification step. Deneddylation was conducted in 20 mM Tris HCl, pH 8.0, 200 mM NaCl and 5 mM DTT without elution of the Nedd8-Cul1-Rbx1 (approximately 60 kDa) from GST-beads. Samples were taken after incubation at 37 °C for indicated times, boiled in sample buffer and analyzed by western hybridization with indicated antibodies.

2.2. Electron microscopy

2.2.1. Data acquisition

For negative-staining, CSN particles were applied on carbon coated copper grids, incubated for 1 min, washed 2× with buffer (20 mM Tris, 0.5 mM DTT, 20 mM KCl, pH 7.2) and subsequently stained with 2% uranyl acetate. Images were collected at 200 kV at a TecnaiF20 electron microscope equipped with an Eagle camera (pixel size 15 μm, magnification 84271×). For cryo-EM, CSN complexes were incubated on ice for 1 min on Quantifoil 2/1 or 3.5/1 grids that carried an additional carbon film. Subsequently, grids were mounted, washed with buffer and plunged. Focal pairs were recorded at 200 kV (TecnaiF20, magnification 84271×, pixel size on object level 0.178 nm) and under low-dose conditions with approx. 15 $e^{-}/Å^2$ (Fig. S1). Negative stain tilt series were recorded at a magnification of 67873× (tilt range −60° to +60°, angular increment 3°). In total 5 tilt series were recorded at a target defocus of −2 μm.

2.2.2. Image processing

Micrographs were visually screened for drift, astigmatism, and visibility of Thon rings in the power spectrum. The contrast transfer function was determined and micrographs were deconvoluted by phase flipping using the TOM-software [20]. Particles were either detected using the "swarm"-option in EMAN2 [21] or by using a low-resolution reference as search model. Particles detected with a search reference were subsequently inspected in EMAN2. In cryo-images, the positions of the particles were determined on the far-from-focus images and particles were extracted from the close-to-focus images; focal pairs were aligned using EMAN1 [21]. All particle stacks were submitted to reference-free alignment via maximum likelihood classification (ML2D, XMIPP) in order to detect contaminations, overlapping particles, etc. and to remove them from the data-sets. The remaining particle stacks contained 61236 (*Hs*CSN/negatively stained), 51105 (*Mm*CSN/negatively stained), 61235 (*Hs*CSN/ice-embedded), and 98865 (*Mm*CSN/ice-embedded) particles, respectively. 3D-reconstruction was performed in XMIPP [22]. As initial models either the average of aligned subtomograms of negatively stained *Mm*CSN particles (see below) or a model computed from the available high resolution data of Lid/CSN, which was filtered extensively (see Fig. 3C, 4B and C) was used. The resolution ($FCS_{0.5}$) was estimated by separating the particles assigned to each class into an odd and even half, reconstructing the respective 3D-structures and computing the FSC (Fig. S2). Visualization and docking was performed in UCSF Chimera [23]. All image analysis steps were performed with particle images rescaled to a pixel size of 0.356 nm.

Image processing of the tomograms was performed using the tom-toolbox [20]. In order to obtain a search model for the detection of particle positions in the tomograms, 145 particles were selected manually from one of the tilt series. One of the particle volumes was used as initial reference for the alignment of the remaining particles, and the resulting average was subsequently used as search template for the screening of all tomograms. Particle positions were confirmed by visual inspection. In total, 1704 particles were extracted in 64×64×64 boxes (1× binning, resulting pixel size 0.441 nm). Alignment of the particle-volumes was performed in Pytom [24].

2.2.3. Accession numbers

The accession numbers for the 3D models of native human and mouse CSN complexes at the Electron Microscopy Data Bank (EMDB) are: EMD-2569 (*Hs*CSN/negatively stained), EMD-2570 (*Mm*CSN/negatively stained), and EMD-2571 (*Hs*CSN/ice-embedded).

3. Results and discussion

3.1. CSN complexes isolated from human erythrocytes and mouse B8 fibroblasts possess comparable deneddylating activity

In our experiments CSN complexes from two different sources were compared: first, CSN, purified from human erythrocytes [15] and second, CSN, pulled down from Flag-CSN2-B8 mouse fibroblasts [14]. For quality control, CSN preparations were characterized by mass spectrometry and by Western blotting [14,15,25,26]. In the CSN complexes from both origins all eight CSN subunits were found in approximately stoichiometrical amounts. For monitoring deneddylating activity in an *in vitro* assay, initially, we searched for a suitable substrate. Data shown

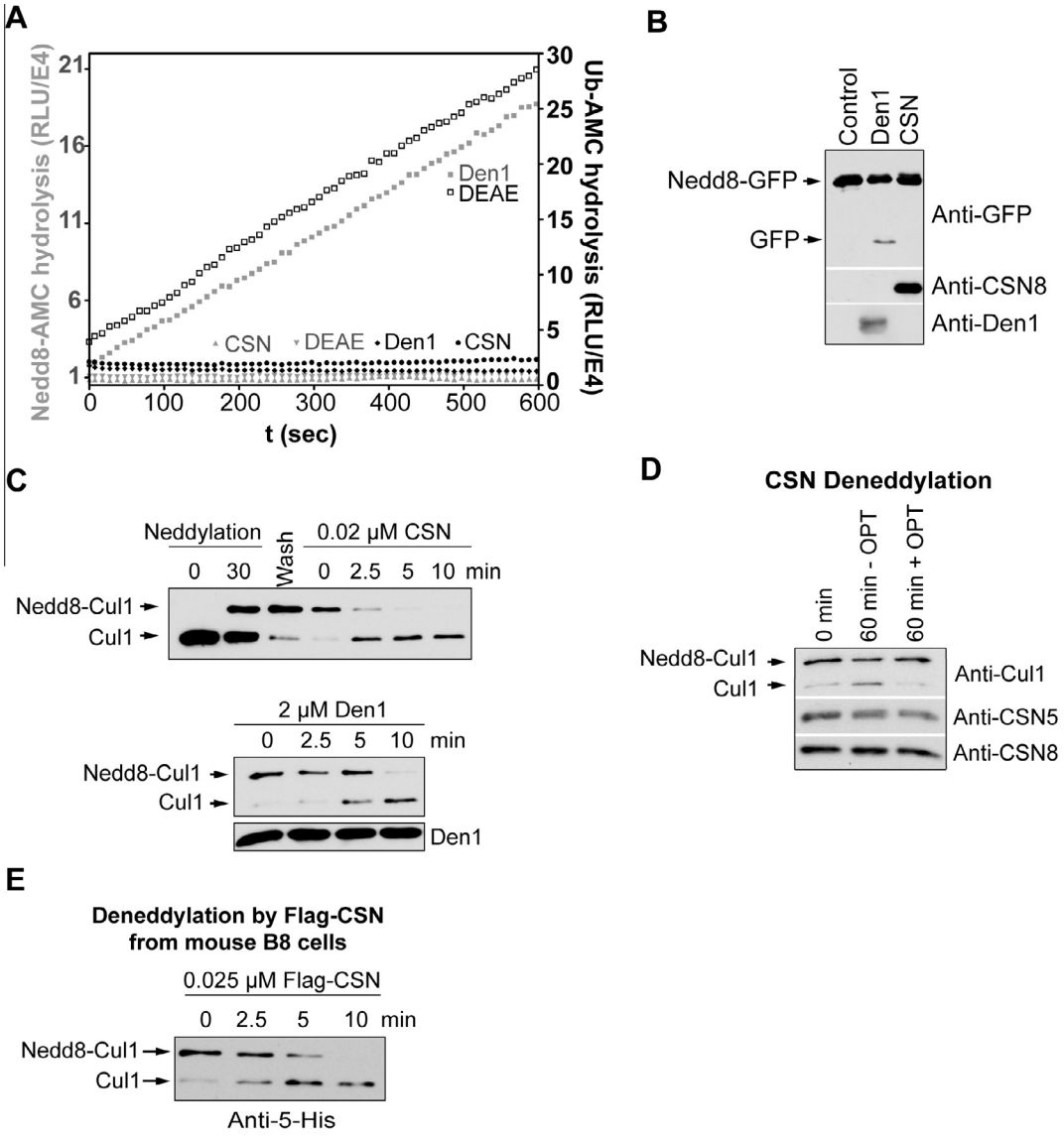

Fig. 1. Comparison of deneddylating activity of CSN complexes obtained from human erythrocytes and mouse B8 fibroblasts using an *in vitro* deneddylation assay. (A) The substrates Ub-AMC (gray scale, left site) and Nedd8-AMC (black scale, right site) were tested in the presence of the CSN, a pool obtained after the DEAE step of CSN preparation from human erythrocytes [15] and recombinant Den1 as another known deneddylase. Fluorescence caused by hydrolysis of the fluorogenic polypeptides (2 μM) was measured at Ex = 380 nm and Em = 460 nm for 10 min at room temperature. (B) Linear Nedd8-GFP fusion protein was incubated with Den1 (2 μM) and with purified CSN (2 μM). Incubations were carried out for 30 min at 37 °C. (C) Cleavage of the substrate Nedd8-Cul1 by CSN (0.02 μM) and Den1 (2 μM). The reaction was carried out at room temperature for indicated time. Upper panel, left site, shows *in vitro* neddylation plus washing of the Nedd8-Cul1 construct. (D) Deneddylation of Nedd8-Cul1 by the CSN purified from human erythrocytes can be inhibited by 5 mM OPT. The reaction was carried out at 37 °C. (E) Cleavage of Nedd8-Cul1 by Flag-CSN complex (0.025 μM) pulled down from mouse B8 fibroblasts.

in Fig. 1A demonstrate that purified human CSN was not able to cleave Ub-AMC under our conditions. This is also true for recombinant deneddylase 1 (Den1), which was used as an additional deneddylating enzyme for comparison. In contrast, the DEAE pool, which was obtained during the preparation of the CSN [15] and which was most likely contaminated with all kinds of deubiquitinating enzymes, cleaved Ub-AMC very efficiently. As expected, Den1 specifically hydrolyzed Nedd8-AMC in contrast to the purified CSN and the DEAE pool. Our data confirm earlier observations on the specificity of Den1 to Nedd8 [27] and show that the CSN cleaved neither Ub- nor Nedd8-AMC [28]. Therefore, we tested another potential substrate, the linear fusion protein Nedd8-GFP. As seen in Fig. 1B, Nedd8-GFP was hydrolyzed by Den1 but not by the human CSN, an observation also described in former studies [28].

Since neither fluorogenic polypeptides nor the linear Nedd8-fusion protein were appropriate substrates for the CSN, neddylated Cul1 was produced using recombinant Cul1-Rbx1 construct [19,29]. The disappearance of neddylated C-terminal 5-His-Cul1/Rbx1 (Nedd8-Cul1) and the formation of deneddylated C-terminal 5-His-Cul1/Rbx1 (Cul1) were visualized by Western blotting using the anti-5-His antibody (Fig. 1C). Obviously, 0.02 μM CSN cleaved Nedd8-Cul1 more efficiently as compared to 2 μM Den1. To control specificity of the reaction, cleavage of Nedd8-Cul1 by the purified CSN was inhibited by 5 mM of the metalloprotease inhibitor o-phenanthroline (OPT) leading to a complete block of deneddylation (Fig. 1D). Our results underline the high specificity of the CSN for the cleavage of Nedd8-Cul1. In addition, the CSN is much more efficient than Den1 in cleaving Nedd8-Cul1, making a simple substitution of CSN by Den1 unlikely [17].

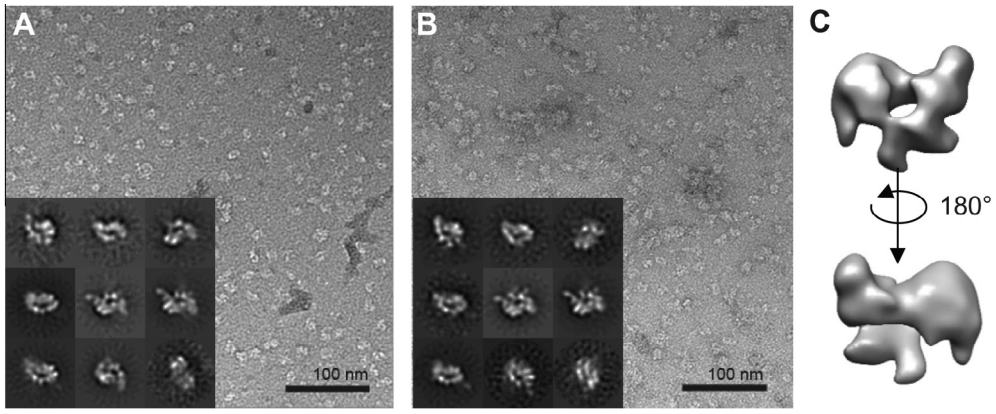

Fig. 2. Negative-stain analysis of CSN complexes from mouse fibroblasts and human erythrocytes. (A and B) Negatively stained CSN particles from human erythrocytes (A) and mouse fibroblasts (B) with corresponding class averages as insert. (C) Initial 3D-model of mouse CSN obtained by single-particle electron tomography.

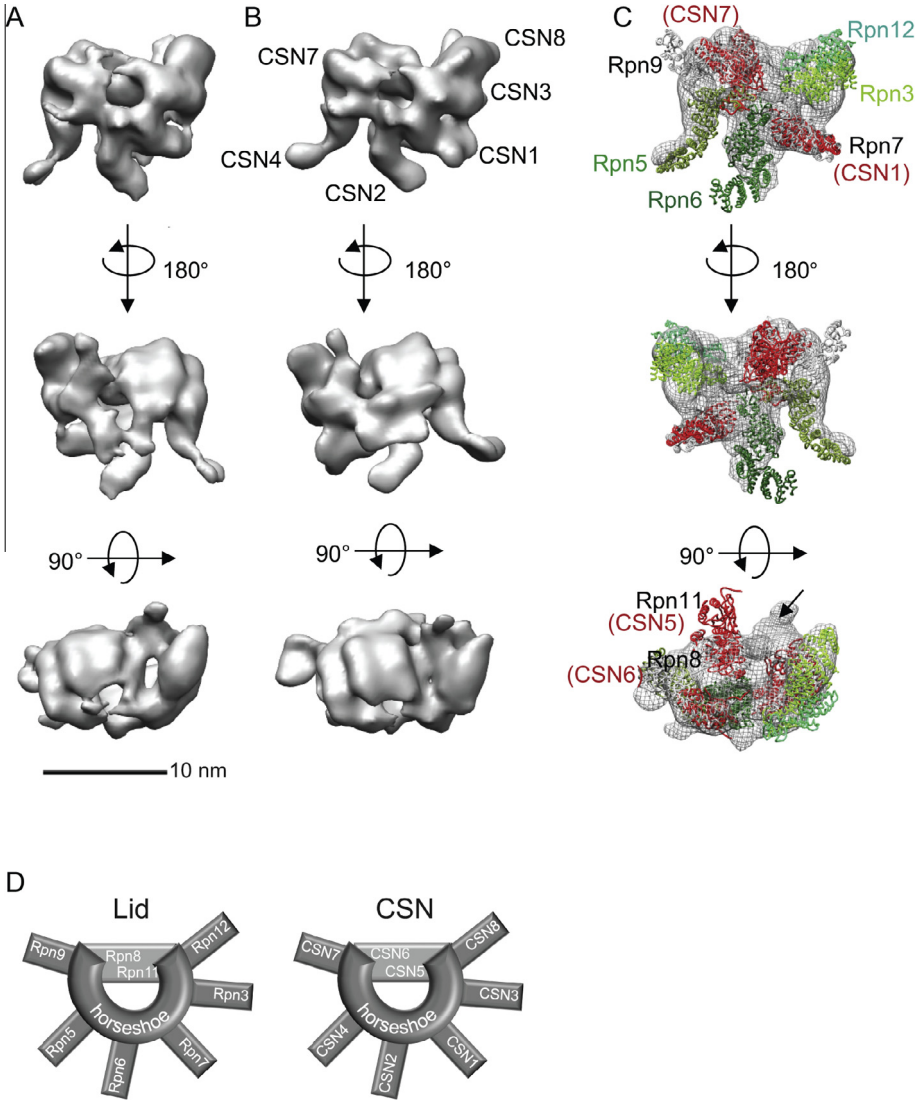

Fig. 3. 3D-reconstructions of negatively stained native CSN complexes. (A and B) 3D-models of native human and mouse CSN, respectively. (C) Overlay of the high resolution structure of the 26S proteasome Lid (ribbon model, PDB-entry: 4B4T) with the negative-stain envelope of human CSN in "front view" (shown as mesh). Ribbon models shown in red are the high resolution models of CSN subunits CSN1 (PDB-entry: 4LCT), CSN4 (PDB-entry: 1UFM), CSN5 (PDB-entry: 4F7O), CSN6 (PDB-entry: 4E0Q), CSN7 (PDB-entry: 3CHM) docked at their position in the EM-envelope, which were selected according to their homology to the respective Lid subunits. Upper panels "front views", middle panels "back views", lower panels "top-view" (rotated by 90° about the horizontal axis). Note that compared to the Lid subunit Rpn9, the N-terminus of CSN7 lacks a number of helical repeats (see also [5]), which flank the winged helix in both subunits. (D) Models of the Lid and the CSN complexes. (For interpretation of the references to color in this figure legend, the reader is referred to the web version of this article.)

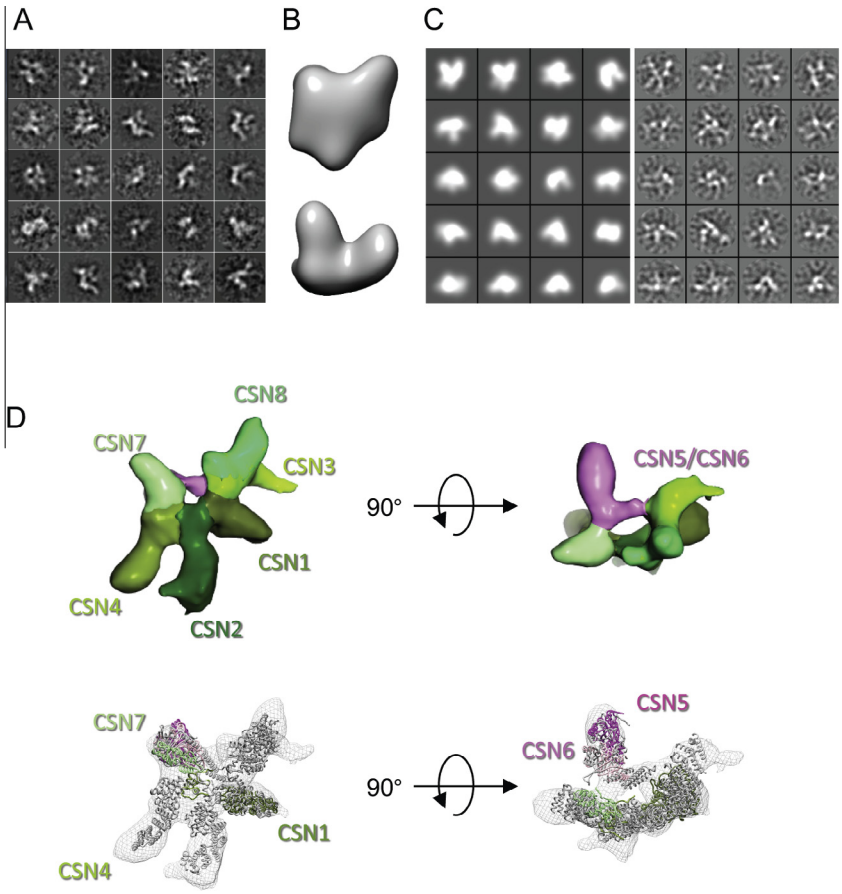

Fig. 4. Cryo-EM of native mammalian CSN complexes. (A) Gallery of class averages obtained by maximum likelihood classification. (B) Initial reference for ML3D alignment constructed from the available high-resolution data of CSN and Lid (see also Fig. 3C). (C) Projections through the initial reference (left) and through the final 3D-model (right) at an angular spacing of 30°. (D) Cryo-structure of native human CSN. Upper panel: surface-representation, domains are segmented and color coded; lower panel: mesh-representation with ribbon structures of Lid and the CSN subunits, coordinates for CSN subunits are colored, the coordinates for Lid-Rpn9 are not shown. (For interpretation of the references to color in this figure legend, the reader is referred to the web version of this article.)

Then we asked whether Flag-CSN pulled down from mouse B8 fibroblasts has deneddylating activity and, if so, whether it is comparable with the activity of human erythrocyte CSN. In Fig. 1E the deneddylating activity of the Flag-CSN is shown. Data obtained by densitometry indicated that there was no significant difference compared to the deneddylating activity of purified CSN from human erythrocytes (see Fig. 1C), which was characterized by a deneddylation rate of 0.7 pmol/min/pmol CSN. The deneddylation rate of Flag-CSN pulled down from mouse B8 fibroblasts was 0.5 pmol/min/pmol CSN. Kinetic features of our CSN complexes shown here are very similar compared to the kinetic data described by Deshaies and co-workers [13].

3.2. Electron microscopy of the native mammalian CSN

In order to test, whether CSN particles from mouse B8 fibroblasts are a proper alternative to human complexes, we have submitted CSN complexes from both sources to single particle electron microscopy. Negatively stained CSN complexes from human red blood cells [15] and mouse fibroblasts [14] appeared to be similar with regard to particle distribution and the shape of typical class averages (Fig. 2A and B). In order to compare their structures also on a 3D-level, we have subjected both data sets to projection matching using a 3D-model obtained by negative-stain tilt-series of mouse CSN (Fig. 2C) as initial reference (see Section 2). The reconstructions obtained have a resolution of ~1.9 nm and are approximately triangular with a horseshoe structure at the front, from where masses emanate (Fig. 3A and B). At their back, the 3D-models display a segment of a circle that connects the upper two corners of the triangle. To better interpret these structures, we have compared the CSN density with the high resolution structure of the Lid [30]. Based on their homology to the Lid subunits and the localization proposed in earlier structural studies of the CSN [5,6], we have labeled the densities of the negative-stain reconstruction (Fig. 3C). Both mouse and human CSN 3D-structures show the horseshoe formed by subunits CSN1 (Rpn7), CSN2 (Rpn6), CSN3 (Rpn3), CSN4 (Rpn5), CSN7 (Rpn9), CSN8 (Rpn12), which interact via their PCI-domains (see models in Fig. 3D), and they agree well with the high resolution structure of the Lid [30]. However, whereas subunits CSN4, CSN1, CSN3 and CSN8 are well presented, our 3D-reconstructions lack the N-terminal density of CSN2. Also, the density attributed to CSN7 does not extend over a number of helical repeats of the corresponding Lid subunit Rpn9, but in this case the corresponding sequence stretch is not present in CSN7 (Fig. 3C).

In the Lid, Rpn11 (corresponding to CSN5) points away from the horseshoe plane. In our negative-stain reconstructions of CSN there is no room to accommodate CSN5; however, there is unoccupied density at the opposite position of the horseshoe (Fig. 3C, lower row, arrow). This potential dislocation might be a consequence of flattening, potentially occurring in conjugation with negative-stain and prompted us to analyze ice-embedded CSN complexes as well (Fig. S1). With ice-embedded human CSN particles we observed more different class averages than

with negatively stained CSN particles (compare Figs. 2A and B with 4A), which implies that the former might adopt a larger number of different orientations on the EM-grid. Since for further 3D-analysis the average obtained from negatively stained particles appeared not to be a good initial model, we have constructed another starting model using the available high resolution data of Lid/CSN, which we have filtered extensively (see Figs. 3C, 4B). This reference was used for a set of 3D maximum likelihood runs (XMIPP, [22]) and resulted in a 3D-structure of 2.7 nm resolution (Fig. 4D, S2) the projections of which resembled the class averages obtained in the ML2D runs (Fig. 4C).

Albeit they share the same basic features, the cryo-structure of native CSN is more delicate than the negative-stain structure. It consists of a U-shaped central segment from which several arms emanate radially – the horseshoe. At the back, a mass sticks out perpendicularly from the horseshoe-plane. In analogy to the position of the MPN-subunits Rpn11 and Rpn8 in the Lid, this is the likely location for CSN5 and CSN6. Also at the back, the two ends of the horseshoe are connected by an elongated mass. Compared to the negative-stain structure, the densities assigned to CSN2 and CSN4 appear to be better defined in the cryo-map. In both maps of native CSN, CSN4 is better defined or in a different conformation than in the negative-stain model of recombinant CSN (Fig. S3). Interestingly, the classes obtained with ML3D mainly differ in the shape of the horseshoe. This can be observed in both native CSN complexes isolated from human and from mouse cells (Fig. S2). A kind of unusual horseshoe is also seen in the recently published cryo-structure of eIF3 (Fig. S3 E) [4].

Our structural studies represent a continuation of earlier EM analysis [3]. More than 10 years ago 2D negative-stain EM revealed the first structural model of the purified CSN from human erythrocytes. Recently, Morris and co-workers created first 3D models using single-particle analysis [5,6]. These studies were performed with recombinant CSN complexes. Here, we show the structure of native mammalian CSN complexes isolated from human red blood cells or mouse B8 fibroblasts. Our structures resemble the negative-stain CSN structure recently published by Morris and colleagues albeit there also are some structural differences. Compared to negatively stained CSN particles, CSN particles embedded in ice apparently adopt a wider range of different orientations (Fig. S2), however, this wider range and the large number of particles did not result in higher resolution. Maybe the low signal-to-noise ratio of the particles that were vitrified on a thin carbon film did prevent a successful separation of potentially different CSN conformations. The relatively low resolution of the reconstructions obtained (2.7 nm) does not allow detailed analyzes of the subunit conformations. Still, an interesting observation was the apparent variable conformation of the horseshoe. This raises the question, whether this structural unit is really flexible, and whether factors like phosphorylation might influence its conformation, perhaps for adapting it for specific interactions.

Because CSN subunits are highly conserved, it is not surprising that mouse and human CSN particles possess similar features. However, the two methods of CSN isolation vary significantly and might influence biochemical and structural properties of the particles differently. The purification of the human CSN from outdated erythrocyte concentrate conserves is an elaborated and costly procedure lasting approximately 3 weeks. It includes several chromatographic as well as density gradient steps [15]. The Flag-CSN pulldown is less expensive and takes only 3 days. Because biochemical and structural results obtained with CSN complexes isolated from human erythrocytes and purified by Flag-CSN pulldown from mouse B8 fibroblasts are very similar, Flag-CSN pulldowns are a proper alternative to purified human erythrocyte complexes.

Acknowledgments

We thank Oana Mihalache for electron microscopy of negatively stained CSN and Dr. Friedrich Förster for helpful discussions. This work has been supported by the Deutsche Forschungsgemeinschaft (DFG) DU 229/9-3 and DU 229/12-2.

Appendix A. Supplementary data

Supplementary data associated with this article can be found, in the online version, at http://dx.doi.org/10.1016/j.bbrc.2014.06.093.

References

[1] G.A. Cope, R.J. Deshaies, COP9 signalosome: a multifunctional regulator of SCF and other cullin-based ubiquitin ligases, Cell 114 (2003) 663–671.
[2] M.W. Schmidt, P.R. McQuary, S. Wee, K. Hofmann, D.A. Wolf, F-box-directed CRL complex assembly and regulation by the CSN and CAND1, Mol. Cell 35 (2009) 586–597.
[3] B. Kapelari, D. Bech-Otschir, R. Hegerl, R. Schade, R. Dumdey, W. Dubiel, Electron microscopy and subunit–subunit interaction studies reveal a first architecture of COP9 signalosome, J. Mol. Biol. 300 (2000) 1169–1178.
[4] J. Querol-Audi, C. Sun, J.M. Vogan, M.D. Smith, Y. Gu, J.H. Cate, E. Nogales, Architecture of human translation initiation factor 3, Structure 21 (2013) 920–928.
[5] R.I. Enchev, A. Schreiber, F. Beuron, E.P. Morris, Structural insights into the COP9 signalosome and its common architecture with the 26S proteasome lid and eIF3, Structure 18 (2010) 518–527.
[6] R.I. Enchev, D.C. Scott, P.C. da Fonseca, A. Schreiber, J.K. Monda, B.A. Schulman, M. Peter, E.P. Morris, Structural basis for a reciprocal regulation between SCF and CSN, Cell Rep. 2 (2012) 616–627.
[7] K. Lasker, F. Forster, S. Bohn, T. Walzthoeni, E. Villa, P. Unverdorben, F. Beck, R. Aebersold, A. Sali, W. Baumeister, Molecular architecture of the 26S proteasome holocomplex determined by an integrative approach, Proc. Natl. Acad. Sci. U.S.A. 109 (2012) 1380–1387.
[8] G.C. Lander, E. Estrin, M.E. Matyskiela, C. Bashore, E. Nogales, A. Martin, Complete subunit architecture of the proteasome regulatory particle, Nature 482 (2012) 186–191.
[9] G.A. Cope, G.S. Suh, L. Aravind, S.E. Schwarz, S.L. Zipursky, E.V. Koonin, R.J. Deshaies, Role of predicted metalloprotease motif of Jab1/Csn5 in cleavage of Nedd8 from Cul1, Science 298 (2002) 608–611.
[10] A. Echalier, Y. Pan, M. Birol, N. Tavernier, L. Pintard, F. Hoh, C. Ebel, N. Galophe, F.X. Claret, C. Dumas, Insights into the regulation of the human COP9 signalosome catalytic subunit, CSN5/Jab1, Proc. Natl. Acad. Sci. U.S.A. 110 (2013) 1273–1278.
[11] R. Verma, L. Aravind, R. Oania, W.H. McDonald, J.R. Yates 3rd, E.V. Koonin, R.J. Deshaies, Role of Rpn11 metalloprotease in deubiquitination and degradation by the 26S proteasome, Science 298 (2002) 611–615.
[12] M. Hu, P. Li, M. Li, W. Li, T. Yao, J.W. Wu, W. Gu, R.E. Cohen, Y. Shi, Crystal structure of a UBP-family deubiquitinating enzyme in isolation and in complex with ubiquitin aldehyde, Cell 111 (2002) 1041–1054.
[13] E.D. Emberley, R. Mosadeghi, R.J. Deshaies, Deconjugation of Nedd8 from Cul1 is directly regulated by Skp1-F-box and substrate, and the COP9 signalosome inhibits deneddylated SCF by a noncatalytic mechanism, J. Biol. Chem. 287 (2012) 29679–29689.
[14] X. Huang, B.K. Hetfeld, U. Seifert, T. Kahne, P.M. Kloetzel, M. Naumann, D. Bech-Otschir, W. Dubiel, Consequences of COP9 signalosome and 26S proteasome interaction, FEBS J. 272 (2005) 3909–3917.
[15] B.K. Hetfeld, D. Bech-Otschir, W. Dubiel, Purification method of the COP9 signalosome from human erythrocytes, Methods Enzymol. 398 (2005) 481–491.
[16] H.H. Chang, M.K. Guo, F.H. Kasten, M.C. Chang, G.F. Huang, Y.L. Wang, R.S. Wang, J.H. Jeng, Stimulation of glutathione depletion, ROS production and cell cycle arrest of dental pulp cells and gingival epithelial cells by HEMA, Biomaterials 26 (2005) 745–753.
[17] M. Christmann, T. Schmaler, C. Gordon, X. Huang, O. Bayram, J. Schinke, S. Stumpf, W. Dubiel, G.H. Braus, Control of multicellular development by the physically interacting deneddylases DEN1/DenA and COP9 signalosome, PLoS Genet. 9 (2013) e1003275.
[18] M. Abdelrahim, S. Safe, Cyclooxygenase-2 inhibitors decrease vascular endothelial growth factor expression in colon cancer cells by enhanced degradation of Sp1 and Sp4 proteins, Mol. Pharmacol. 68 (2005) 317–329.
[19] D.M. Duda, L.A. Borg, D.C. Scott, H.W. Hunt, M. Hammel, B.A. Schulman, Structural insights into NEDD8 activation of cullin-RING ligases: conformational control of conjugation, Cell 134 (2008) 995–1006.
[20] S. Nickell, F. Forster, A. Linaroudis, W.D. Net, F. Beck, R. Hegerl, W. Baumeister, J.M. Plitzko, TOM software toolbox: acquisition and analysis for electron tomography, J. Struct. Biol. 149 (2005) 227–234.
[21] G. Tang, L. Peng, P.R. Baldwin, D.S. Mann, W. Jiang, I. Rees, S.J. Ludtke, EMAN2: an extensible image processing suite for electron microscopy, J. Struct. Biol. 157 (2007) 38–46.

[22] S.H. Scheres, R. Nunez-Ramirez, C.O. Sorzano, J.M. Carazo, R. Marabini, Image processing for electron microscopy single-particle analysis using XMIPP, Nat. Protoc. 3 (2008) 977–990.
[23] E.F. Pettersen, T.D. Goddard, C.C. Huang, G.S. Couch, D.M. Greenblatt, E.C. Meng, T.E. Ferrin, UCSF Chimera – a visualization system for exploratory research and analysis, J. Comput. Chem. 25 (2004) 1605–1612.
[24] T. Hrabe, Y. Chen, S. Pfeffer, L.K. Cuellar, A.V. Mangold, F. Forster, PyTom: a python-based toolbox for localization of macromolecules in cryo-electron tomograms and subtomogram analysis, J. Struct. Biol. 178 (2012) 177–188.
[25] S. Rozen, A. Tieri, G. Ridner, A.K. Stark, T. Schmaler, G. Ben-Nissan, W. Dubiel, M. Sharon, Exposing the subunit diversity within protein complexes: a mass spectrometry approach, Methods 59 (2013) 270–277.
[26] T. Schmaler, W. Dubiel, Control of deneddylation by the COP9 signalosome, Subcell. Biochem. 54 (2010) 57–68.
[27] L.N. Shen, H. Liu, C. Dong, D. Xirodimas, J.H. Naismith, R.T. Hay, Structural basis of NEDD8 ubiquitin discrimination by the deNEDDylating enzyme NEDP1, EMBO J. 24 (2005) 1341–1351.
[28] K. Wu, K. Yamoah, G. Dolios, T. Gan-Erdene, P. Tan, A. Chen, C.G. Lee, N. Wei, K.D. Wilkinson, R. Wang, Z.Q. Pan, DEN1 is a dual function protease capable of processing the C terminus of Nedd8 and deconjugating hyper-neddylated CUL1, J. Biol. Chem. 278 (2003) 28882–28891.
[29] N. Zheng, B.A. Schulman, L. Song, J.J. Miller, P.D. Jeffrey, P. Wang, C. Chu, D.M. Koepp, S.J. Elledge, M. Pagano, R.C. Conaway, J.W. Conaway, J.W. Harper, N.P. Pavletich, Structure of the Cul1-Rbx1-Skp1-F boxSkp2 SCF ubiquitin ligase complex, Nature 416 (2002) 703–709.
[30] F. Beck, P. Unverdorben, S. Bohn, A. Schweitzer, G. Pfeifer, E. Sakata, S. Nickell, J.M. Plitzko, E. Villa, W. Baumeister, F. Forster, Near-atomic resolution structural model of the yeast 26S proteasome, Proc. Natl. Acad. Sci. U.S.A. 109 (2012) 14870–14875.